Vertical distribution of HMXBs in NGC 55: constraining their centre-of-mass velocity

Babis Politakis,[1,2]★ Andreas Zezas,[1,2,3]★ Jeff J. Andrews [2,4]★
and Stephen J. Williams[2,5]

[1]*Department of Physics, University of Crete, Heraklion 71003, Greece*
[2]*Foundation for Research and Technology - Hellas (FORTH), Heraklion 71003, Greece*
[3]*Harvard-Smithsonian Center for Astrophysics, Cambridge, MA 02138, USA*
[4]*Niels Bohr Institute, University of Copenhagen, Blegdamsvej 17, DK-2100 Copenhagen, Denmark*
[5]*USNO – 3450 Massachusetts Ave, NW, Washington, DC 20392–5420, USA*

ABSTRACT

We analyse the vertical distribution of high-mass X-ray binaries (HMXBs) in NGC 55, the nearest edge-on galaxy to the Milky Way (MW), based on X-ray observations by *Chandra*. Adopting a statistical approach, we estimate the difference between the scale height of the vertical distribution of HMXBs and the vertical distribution of star-forming activity between 0.33 and 0.57 kpc. The spatial offsets can be explained by a momentum kick the X-ray binaries receive during the formation of the compact object after a supernova explosion of the primary star. Determining the vertical distribution of HMXBs in the MW using *Gaia* DR2 astrometry, we find that the corresponding difference is considerably lower at 0.036 ± 0.003 kpc, attributed to the greater gravitational potential of the MW. We also calculate the centre-of-mass transverse velocities of HMXBs in NGC 55, using traveltime information from binary population synthesis codes and for different star formation histories (SFHs). For a flat SFH model (typical of spiral galaxies like NGC 55), we find that HMXBs are moving with a typical transverse velocity between 34 and 48 km s^{-1}, consistent with space velocities of MW HMXBs. For an exponentially declining SFH model, HMXBs are moving at a velocity of 21 km s^{-1}, consistent with the corresponding velocity of HMXBs in the Small Magellanic Cloud and Large Magellanic Cloud. Finally, we estimate the formation efficiency of HMXBs in NGC 55 at 299^{+50}_{-46} (systems/M$_\odot$ yr^{-1}), consistent within the errors with the Magellanic Clouds but significantly higher than the MW, a difference that can be explained by the subsolar metallicity of NGC 55.

Key words: X-rays: stars – binaries: close.

1 INTRODUCTION

High-mass X-ray binaries (HMXBs) are among the brightest sources of X-ray emission in galaxies. They are close binary systems comprised of a compact object (neutron star or black hole – the primary star of the system) and a non-degenerate massive companion star (secondary star of the system) with a mass above $\sim$8 M$_\odot$ (Bhattacharya & van den Heuvel 1991). The observed X-ray emission is powered either by accretion of wind material or mass transfer through stable Roche lobe overflow from the companion star to the compact object. Wind-fed HMXBs are further divided into SG-XRBs (the companion star is an O/B supergiant) and Be-XRBs (the companion star is an Oe/Be-type star).

In SG-XRBs, the companions are stars of luminosity class I–II, with mass-loss rates between 10^{-6} and 10^{-8} M$_\odot$ yr^{-1}. A neutron star or a black hole in a close orbit (<15 d; Liu, van Paradijs & van den Heuvel 2006) will capture some fraction of this wind, sufficient to power a bright X-ray source. In Be-XRBs, the companions are non-supergiant, fast-rotating O/B-type stars of luminosity class III–V, which at some point of their lives have shown spectral lines in emission (Reig 2011). The origin of the emission lines is attributed to an equatorial disc, fed from material expelled from the rapidly rotating Be-star (Porter & Rivinius 2003). X-ray outbursts are expected when the compact object passes through the Be-star disc, accreting from the low-velocity and high-density wind (Okazaki, Hayasaki & Moritani 2013). Mass transfer rates from systems

★ E-mail: hpolitak@physics.uoc.gr (BP); azezas@physics.uoc.gr (AZ); andrews@physics.uoc.gr (JJA)

undergoing stable Roche lobe overflow are typically a few orders of magnitude higher than their wind-fed analogues, resulting in the formation of an accretion disc around the compact object, with generally higher X-ray luminosities compared to wind-fed systems.

Although HMXBs are typically associated with star-forming regions (Grimm, Gilfanov & Sunyaev 2003; Fabbiano 2006; Persic & Rephaeli 2007), such as galaxy spiral arms and massive, young stellar clusters, there is observational evidence for a population of HMXBs that are somewhat offset from star-forming regions (van Rensbergen, Vanbeveren & De Loore 1996; Zezas et al. 2002; Kaaret et al. 2004). The observed displacement may be due to kicks after an asymmetric supernova (SN) explosion during the formation of the compact object (e.g. Fryer & Kalogera 1997). These kicks have fundamental implications for the population of X-ray binaries since they determine the survival and the post-SN orbital parameters of the system (Pfahl et al. 2002; Podsiadlowski et al. 2004). If they are large enough, kicks will extend the vertical distribution of HMXBs, which can potentially be measured in nearby edge-on galaxies with high angular resolution X-ray telescopes. The extended vertical distribution of HMXBs can be used to estimate the transverse velocity of the binary systems, provided their age of is known.

These measurements are so far limited to the Magellanic Clouds (MCs) and the Milky Way (MW). For the Large Magellanic Cloud (LMC) the typical transverse velocities are 12.4 ± 7.0 km s^{-1} for SG-XRBs and 10.8 ± 7.3 km s^{-1} for Be-XRBs (Antoniou & Zezas 2016). For the Small Magellanic Cloud (SMC), where almost all HMXBs are Be-XRBs, the typical transverse velocities are 16 km s^{-1} (Coe 2005) and 13.1 km s^{-1} (Antoniou & Zezas 2016). For the MW, the average transverse velocity of Be-XRBs is comparable with the MCs at 15 ± 6 km s^{-1}, while the SG-XRB population has a higher average transverse velocity of 42 ± 14 km s^{-1} (van den Heuvel et al. 2000).

NGC 55, the edge-on galaxy nearest to the MW at a distance of 1.94 Mpc (Gieren et al. 2008) provides an excellent environment for studying the relation between HMXBs and star-forming regions. NGC 55 with a total mass of 2×10^{10} M$_\odot$ (Westmeier, Koribalski & Braun 2013) is classified as an SB(s)m galaxy viewed at an inclination of 80 deg with an optical extent of 18.2×3.2 kpc (de Vaucouleurs et al. 1991). The optical morphology of NGC 55 is asymmetric, with the brightest region of the galactic disc located at 1.7 kpc west from the geometrical centre of the galaxy and along the galactic plane (de Vaucouleurs et al. 1991). The main properties of NGC 55 are presented in Table 1.

In the following sections of this paper, we first present the X-ray source catalogue used in this work (Section 2). In Section 3 we calculate the vertical distribution of HMXBs with reference to the projected mid-plane of NGC 55 and estimate their average displacement from the star-forming regions as well as their centre-of-mass transverse velocity. In Section 4 we discuss our results and we conclude in Section 5.

2 THE HMXB POPULATION IN NGC 55

The population of X-ray sources in NGC 55 has been analysed as part of the Chandra Local Volume Survey (Binder et al. 2015) using archival ACIS data from the *Chandra* X-ray Observatory (ObsIDs 2255 and 4744). The source list consists of 154 X-ray sources down to a flux of 7×10^{-16} erg s^{-1} cm^{-2} ($L_x = 0.3 \times 10^{36}$ erg s^{-1} at a distance of 1.94 Mpc). Binder et al. (2015) classified the X-ray sources on the basis of either their optical associations with stars using *Hubble Space Telescope* (*HST*) fields selected from the

Table 1. NGC 55 properties.

| Parameter	Value
Morphological type	SB(s)m: edge-on[a]
RA (hh:mm:ss)	00:14:53.60[b]
Dec. ($\pm$ dd:mm:ss)	-39:11:47.9[b]
Distance (Mpc)	1.94 ± 0.03[c]
Major axis (2a arcsec; kpc)	1942; 18.2[a]
Minor axis (2b arcsec; kpc)	338; 3.2[a]
Position angle (deg)	108[a]
Inclination (deg)	80[a]
$E(B - V)$ (mag)	0.01[d]
Radial velocity (km s^{-1})	131 ± 2[e]
Rotational velocity (km s^{-1})	90.6 ± 2.5[e]
Stellar mass (M$_\odot$)	1.9×10^{9}[k]
HI mass (M$_\odot$)	$(1.7 \pm 0.1) \times 10^{9}$[e]
Total mass (M$_\odot$)	$(2.0 \pm 0.4) \times 10^{10}$[e]
$L_{\rm TIR}$ (L$_\odot$) (3–1100 μm)	1.6×10^{9}[d]
SFR (M$_\odot$ yr^{-1})	$0.137^{+0.023}_{-0.021}$[f]
Metallicity [Fe/H]	-0.3[g]
Scale height$_{\rm FarIR}$ (kpc)	0.32–0.49[h]
Scale height optical$_{\rm F818W}$ (kpc)	0.24[i]
Scale height$_{{\rm H}\alpha}$ (kpc)	0.37–0.45[j]

[a]de Vaucouleurs et al. (1991); [b]Jarrett (2000); [c]Gieren et al. (2008); [d]Dale et al. (2009); [e]Westmeier et al. (2013); [f]Weisz et al. (2011); [g]Davidge (2005); [h]Engelbracht et al. (2004); [i]Seth, Dalcanton & de Jong (2005); [j]Miller & Veilleux (2003); [k]Kudritzki et al. (2016).
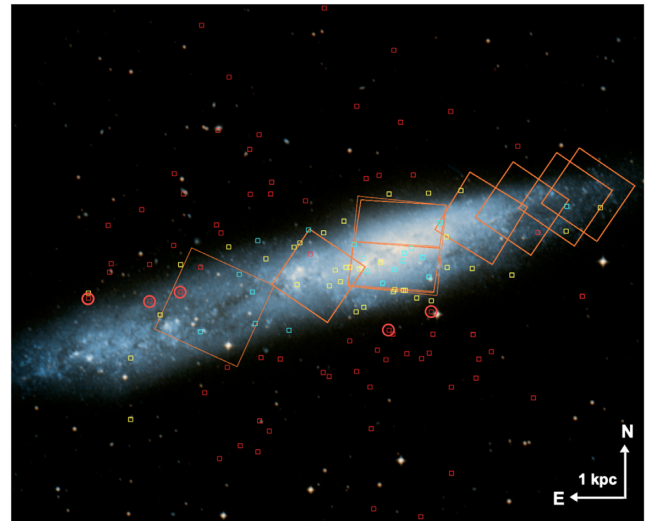
Figure 1. Population of X-ray sources in NGC 55 superimposed on a *GALEX* NUV (2267 Å) image (Gil de Paz et al. 2007). The X-ray sources are colour-coded as follows: Candidate and verified HMXBs in yellow and cyan respectively (Section 2), AGNs in red (Binder et al. 2015). The footprints of the *HST* fields are shown as orange boxes. The five AGNs encircled in red were initially classified as HMXBs (Binder et al. 2015) but based on our analysis in Section 2, we reclassify these as background AGNs.

ACS Nearby Galaxy Survey Treasury (Dalcanton et al. 2009) or their X-ray properties (hardness ratios): 65 as active galactic nuclei (AGNs), 10 as foreground stars, 11 as SN remnants, and 67 as XRBs, among which 24 as low-mass X-ray binaries (LMXBs) and 43 as HMXBs.

Fig. 1 shows the location of XRBs and AGN superimposed on a *GALEX* NUV (2267 Å) image (Gil de Paz et al. 2007). The
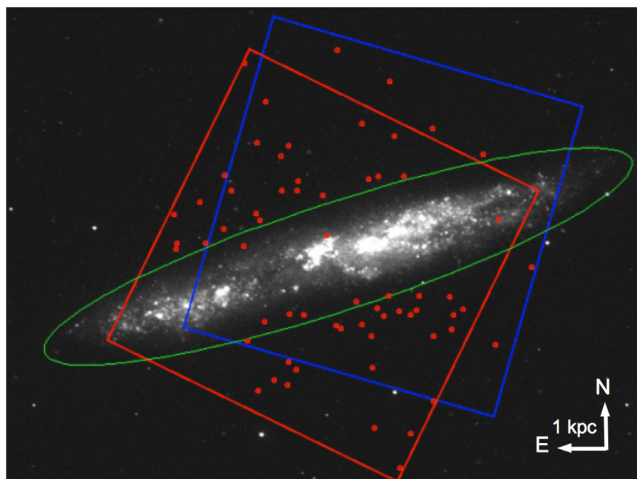
Figure 2. Location of AGNs (red circles) in the *Chandra* FOV for ObsID 2255 (red) and ObsID 4744 (blue). The D_{25} of NGC 55 is shown as a green ellipse. The number counts of background AGNs far off the plane of NGC 55 are used for empirically determining the AGN density within the *Chandra* FOV.

sources are colour-coded according to their classification by Binder et al. (2015): XRBs in yellow and cyan (for candidate and verified HMXBs respectively, see Table 3), while background AGN in red. The footprints of the *HST* fields are shown with the orange boxes. Only 16 of the 43 X-ray sources classified as HMXBs have optical counterparts identified using *HST* data. The other 27 HMXB candidates extend beyond the *HST* fields and were classified based on X-ray hardness ratios alone, making them much less certain.

We first examine if the population of XRBs as classified by Binder et al. (2015) is contaminated with background AGN. We use the cumulative number counts of X-ray point sources published in the Chandra Multiwavelength Project (ChaMP; Kim et al. 2007) and derive approximately 1000 AGN deg^{-2} down to the limiting flux of the *Chandra* observations for NGC 55. Fig. 2 shows the *Chandra* field of view (FOV) for ObsID 2255 (red) and ObsID 4744 (blue). The FOV covers an area of 0.078 deg^2, therefore the expected number of AGNs based on ChaMP is approximately 78.

Alternatively, the AGN density can be determined empirically from the number counts of background AGN in regions far off the plane of NGC 55, since most of the X-ray sources close to the plane and within the D_{25} (green ellipse in Fig. 2) are categorized as candidate XRBs. The result for the AGN density is approximately 80 X-ray sources within the *Chandra* FOV, in close agreement with the estimation using the expected AGN number density from ChaMP.

Since there are 59 X-ray sources classified as AGN by Binder et al. 2015 within the *Chandra* FOV for observation 2255, we estimate that there may be ∼20 background AGNs among the 67 sources classified as XRBs.

We also quantify the percentage of contamination by looking at the distribution of all X-ray sources classified as AGNs. A Kolmogorov–Smirnov (K-S) test across vertical bins of 0.1 kpc from the plane derives that at a confidence level of 95 per cent, their distribution does not follow a uniform one. On the other hand, if we exclude the bins corresponding to the D_{25} of the galaxy where most of the X-ray sources are categorized as candidate XRBs and perform a K-S test across the rest of the bins, at a confidence level

of 95 per cent, the distribution of AGN derives from a uniform one. In order to estimate the number of background AGNs among candidate XRBs in the D_{25} region, we modify the distribution of all X-ray sources classified as AGN by adding sources at random locations within the D_{25}. Each time a new source is added, a K-S test across all bins determines if the distribution derives from a uniform one. The number of sources within the D_{25} that are required for the distribution of AGNs to derive to high confidence from a uniform one, is between 14 and 23, in agreement with the previous estimation for ∼20 background AGNs.

We next investigate the characterization of the X-ray sources as HMXBs, by supplementing their classification with mid-IR photometry of NGC 55 from *Spitzer* IRAC (Williams & Bonanos 2016). We cross-match the list of X-ray sources in Binder et al. (2015) with the list of mid-IR sources in Williams & Bonanos (2016) using only those mid-IR sources that have been detected in all four *Spitzer* IRAC channels. This results in 21 matches presented in Table 2, from which 9 are classified as HMXBs and 12 as AGNs in Binder et al. (2015).

In order to identify the contaminating AGNs among the matched HMXB sources, we apply a mid-IR diagnostic that enables the distinction between AGNs and massive stars. The diagnostic we use is the [3.6]–[4.5] versus [5.8]–[8.0] μm colour–colour diagram in which Stern et al. (2005) empirically defined the locus of AGNs (the so-called 'Stern wedge'), delineated by the dashed line in Fig. 3. To check the credibility of the 'Stern wedge' diagnostic we populate the [3.6]–[4.5] versus [5.8]–[8.0] μm diagram with spectroscopically classified massive stars (bottom panel) from nearby galaxies, derived from the catalogues of Williams et al. (2015), Khan et al. (2015) and Castro et al. (2008). We see that the overlap of stars with the AGN locus is very small.

Fig. 3 (top panel) shows the HMXBs (red stars) and AGNs (blue filled circles) with mid-IR counterparts placed on a mid-IR [3.6]–[4.5] versus [5.8]–[8.0] diagram. From the nine sources classified as an HMXB by Binder et al. (2015), five fall within the 'Stern wedge'. Four of these five sources are found at large distances from the plane of NGC 55 (encircled in red in Fig. 1), which decreases the chance that these sources are associated with NGC 55. The four of the nine sources that do not fall within the 'Stern wedge' and the diagnostic suggests are HMXBs, are placed on a mid-IR colour–magnitude diagram (Fig. 4). The similarity of these optical associations with other spectroscopically classified massive O-type, B-type, A-type, and LBV stars in NGC 55 (Castro et al. 2008) further supports the nature of these X-ray sources as HMXBs. From the 12 sources classified as an AGN by Binder et al. (2015), all but one fall within the Stern wedge.

We also investigate the classification by Binder et al. (2015) as HMXBs for those sources with *HST* counterparts. We place them on an *HST* colour–magnitude diagram (Fig. 5) with the absolute magnitude computed using the distance in Table 1 (distance modulus of 26.43 mag). We have also overplotted the 100 and 20 Myr isochrones from the Geneva stellar models (Ekström et al. 2012). After applying a reddening correction of $E(B-V) = 0.01$ (Table 1), all but two HMXBs are bounded by the 100 Myr isochrone. We therefore conclude that the *HST* colour–magnitude diagram is consistent with the classification of the X-ray sources with *HST* counterparts as HMXBs by Binder et al. (2015). We note that due to the low X-ray luminosity ($<10^{37}$ erg s^{-1}) of the aforementioned sources, illumination of the companion star from the accretion disc around the compact object which may affect their location on the colour–magnitude diagram does not pose a problem.

Table 2. Mid-IR properties of X-ray sources.

X-ray source number (1)	RA (2)	Dec. (3)	Classification (4)	Separation (5)	[3.6] (6)	[4.5] (7)	[5.8] (8)	[8.0] (9)
2	00:15:02.1	−39:16:46.2	AGN	0.23	16.27	17.20	16.14	14.85
11	00:14:56.1	−39:16:18.6	AGN	0.26	17.00	16.58	15.60	14.89
60	00:14:29.2	−39:07:52.5	AGN	0.69	17.27	16.31	15.52	14.29
67	00:14:50.6	−39:09:01.1	AGN	0.07	16.51	15.80	15.32	14.31
68	00:14:42.9	−39:06:30.6	AGN	0.54	16.57	16.09	15.20	14.09
90	00:15:19.4	−39:09:18.3	AGN	0.64	18.06	17.48	15.97	15.26
95	00:15:23.8	−39:09:46.8	AGN	0.35	16.37	15.69	14.93	14.14
104	00:15:45.9	−39:10:22.8	AGN	0.43	16.68	16.08	15.74	15.24
108	00:15:39.4	−39:11:47.4	AGN	0.75	18.07	17.18	15.56	14.60
113	00:15:52.1	−39:12:30.6	AGN	0.24	16.08	15.62	15.29	14.54
152	00:15:08.9	−39:16:48.7	AGN	0.10	17.21	16.41	15.58	14.45
34	00:14:16.0	−39:13:47.8	AGN	0.98	17.24	16.66	16.03	14.47
75	00:15:02.7	−39:10:28.8	HMXB	0.64	16.92	16.29	15.76	14.90
79	00:15:04.0	−39:11:53.8	HMXB	0.20	17.12	16.57	15.66	14.29
80	00:15:04.6	−39:10:43.9	HMXB	0.20	16.98	15.84	14.80	13.25
92	00:15:11.9	−39:11:10.8	HMXB	0.54	16.94	16.87	16.03	15.57
101	00:15:20.0	−39:11:37.1	HMXB	0.34	17.82	16.71	14.92	13.91
103	00:15:22.3	−39:11:36.4	HMXB	0.22	17.49	16.76	15.65	15.34
110	00:15:44.3	−39:12:08.9	HMXB	0.11	15.36	14.82	14.34	13.32
130	00:15:33.9	−39:15:11.8	HMXB	0.99	16.90	16.51	13.85	11.45
140	00:15:15.9	−39:15:08.8	HMXB	0.26	17.89	17.37	16.57	16.25

Note. Column description: (1) X-ray source number assigned by Binder et al. (2015) list, (2) RA (hh mm ss.ss) J2000, (3) Dec. (−dd mm ss.ss) J2000, (4) X-ray classification according to Binder et al. (2015), (5) Separation between X-ray and mid-IR sources in arcsec, (6) 3.6 μm mag, (7) 4.5 μm mag, (8) 5.4 μm mag, and (9) 8.0 μm mag

To summarize, of the 67 XRBs identified by Binder et al. (2015), *HST* and *Spitzer* imaging confirms an early-type star as the counterpart to 19 sources, which form our sample of 'verified HMXBs'. For 6 of the remaining 48 XRBs, *HST* imaging suggests that they are LMXBs and are therefore not included in our analysis. That leaves 42 XRBs, for which statistics suggest that as many as 20 may be AGNs. Using IR imaging, we identify 5 of the 42 XRBs as being AGN contaminants. The remaining 37 XRBs, from which as many as 15 (40 per cent) may be AGNs, form our sample of 'candidate HMXBs'.

Furthermore, if we consider the Grimm et al. (2003) relation for the number of expected HMXBs for the NGC 55 SFR (Table 1), we have ~15 HMXBs with L_x brighter than 10^{36} erg s^{-1}. According to Table 3, the number of HMXBs with $L_x > 10^{36}$ erg s^{-1} is 26, 7 in the 'verified HMXBs' sample and 19 in the 'candidate HMXBs' sample. Applying the estimated percentage (40 per cent) for AGN contamination in the 'candidate HMXBs' sample, we determine that the expected number of HMXBs with $L_x > 10^{36}$ erg s^{-1} is ~18.

For the remainder of this work, we consider as HMXBs all 'verified HMXBs' as well as randomly selected combinations of 22 out of 37 'candidate HMXBs', thereby incorporating our estimated AGN contamination.

We note that none of these HMXBs are spectroscopically confirmed, and therefore are all only candidates (even the 'verified' ones). Defining their nature requires further information (X-ray spectra, *HST* imaging, time variability) that is not yet available.

The list of HMXBs is presented in Table 3. Columns 'RA' and 'Dec.' indicate the location of XRBs as provided by Binder et al. (2015). Column '*z*' presents the inclination corrected vertical distance of each XRB from the mid-plane of the galaxy in kpc. Column 'Flux' provides the unabsorbed 0.35–8 keV flux (Binder et al. 2015). Column 'L_x' presents the X-ray luminosity of each XRB in units of 10^{36} erg s^{-1} estimated from the relevant flux and the distance of NGC 55 in Table 1.

3 VERTICAL DISTRIBUTION OF THE HMXB POPULATION IN NGC 55

In this section we measure the vertical distances of HMXBs from the mid-plane of NGC 55, compare their vertical distribution with the distribution of star-forming activity, and estimate the centre-of-mass transverse velocity of the binary systems. We choose to measure the distance of HMXBs from the mid-plane, since due to the distance of NGC 55, the projected density of star-forming regions is too large to allow us to identify the possible birthplace of each individual HMXB among young star clusters or OB associations, as has been done in the SMC (Coe 2005), LMC (Antoniou & Zezas 2016), and the MW (Bodaghee et al. 2012). This is evident in Fig. 6, which shows separate, representative HMXBs (indicated with an X) located at large distances from the mid-plane, superimposed on a starlight continuum subtracted H α image of NGC 55 (Kopsacheili et al. 2020), which traces star-forming regions. Around each HMXB we draw a 1 kpc radius circle (which, assuming a centre-of-mass velocity of 40 km s^{-1}, corresponds to a traveltime of 25 Myr) with the radial vector pointing towards the mid-plane of the galaxy. We cannot correlate individual HMXBs with specific star-forming regions either because there are multiple possible regions or because there is no star-forming region nearby.

3.1 Vertical distance of HMXBs and SFR

We define as the mid-plane of NGC 55, the plane where star formation rate (SFR) peaks. For this reason we use the highest resolution and least absorption-dependent SFR indicator we have available. This is the 8.0 μm IRAC image that traces polycyclic aromatic hydrocarbon emission from the star-forming regions and correlates almost linearly with the SFR if the small contribution from older stellar populations that also emit in the IR is removed
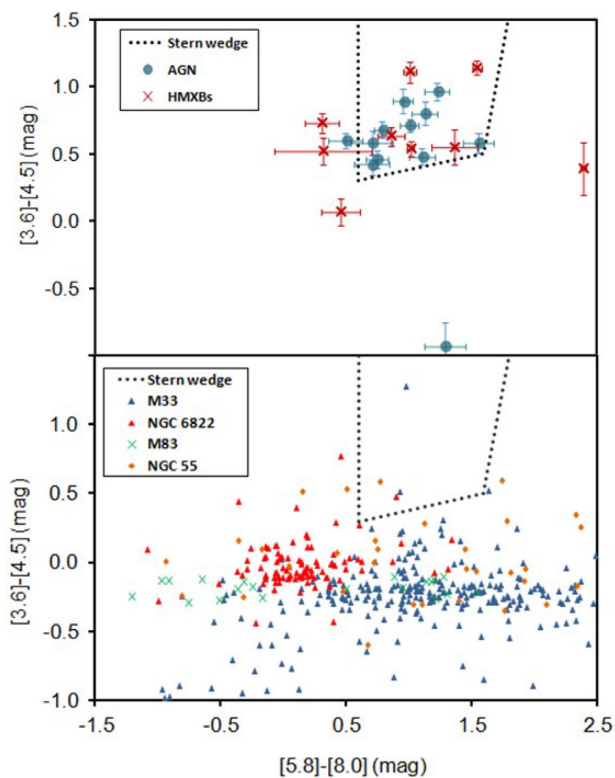
Figure 3. Colour–colour diagram for the identification of AGNs based on mid-IR colours. The dashed line in both panels delineates the AGN locus ('Stern wedge', Stern et al. 2005). Top panel: X-ray sources in NGC55 with mid-IR counterparts. Sources classified as HMXBs (red stars) and AGNs (blue filled circles) according to Binder et al. (2015). Five HMXBs are located within the AGN locus. Bottom panel: to check the credibility of the 'Stern wedge' diagnostic, we populate the [3.6]–[4.5] versus [5.8]–[8.0] µm diagram with spectroscopically resolved massive stars in NGC 55 and other nearby galaxies (Williams et al. 2015; Khan et al. 2015; Castro et al. 2008). Very few massive stars have mid-IR colours consistent with the Stern wedge.

(Calzetti 2008). We use the publicly available SINGS IRAC images of NGC 55 (Dale et al. 2009) and we subtract the 3.6 µm image from the 8.0 µm image using a scaling factor of 0.26 (Wu et al. 2005) in order to remove the contribution from the non-star-forming, stellar populations and create a 'star formation' 8.0 µm image. We then take slices with length equal to the major axis of NGC 55, at an angle equal to the position angle of NGC 55 at 108 deg (de Vaucouleurs et al. 1991; Table 1). The thickness of each slice is 1.98 arcsec, equal to the full width at half-maximum of *Spitzer*'s IRAC band 4 PSF.[1] We take as many slices as required to fully cover the extent of NGC 55 as defined by the D_{25} (Fig. 2) and measure the surface brightness in each slice. The slice with the highest surface brightness is selected as the mid-plane of NGC 55 and is shown as the red line in all panels in Fig. 8.

We measure the vertical distribution of the SFR density from the star-forming 8.0 µm image calculated in bins of the same size as in the case of HMXBs (the yellow histogram in Fig. 7). We model the SFR density with an exponential profile:

$$S(z) = S_0 e^{-z/z_{sfr}}, \tag{1}$$

[1](http://irsa.ipac.caltech.edu/data/SPITZER/docs/irac/iracinstrumenthandbook/)
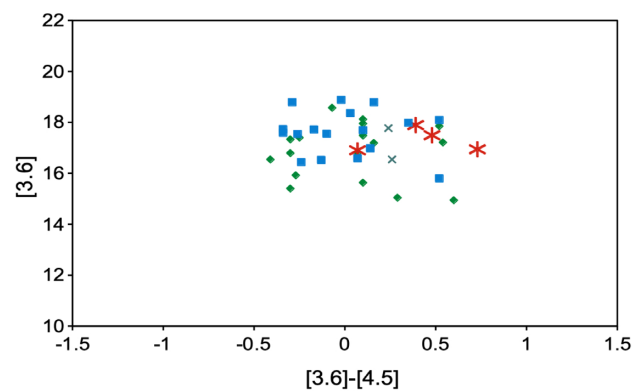
Figure 4. Mid-IR colour–magnitude diagram for spectroscopically classified massive stars in NGC 55 (Castro et al. 2008). The similarity of the IR colours between the four X-ray sources (magenta stars) falling outside the Stern wedge in the top panel of Fig. 3 and the reference stars further supports their classification as HMXBs by Binder et al. (2015).
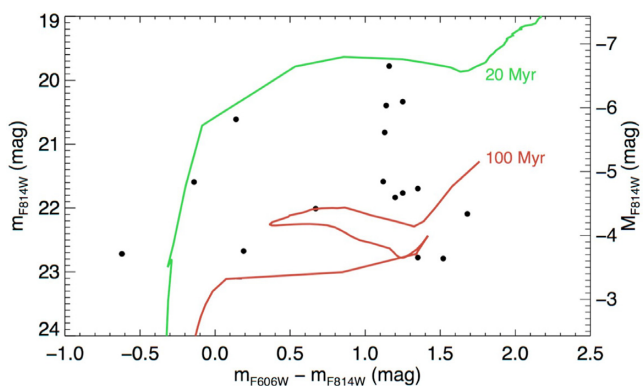
Figure 5. Reddening corrected *HST* colour–magnitude diagram of the optical counterparts of the X-ray sources (black dots) classified as HMXBs by Binder et al. (2015). 20 and 100 Myr isochrones from the Geneva stellar models (Ekström et al. 2012) are overplotted for reference. All but three stars are bounded by the 100 Myr isochrone, confirming their young age and the classification of the X-ray sources by Binder et al. (2015) as HMXBs.

where $S(z)$ is the surface brightness along the z-axis, S_0 is the surface brightness at the mid plane of the galaxy, and z_{sfr} is the vertical scale height. Fitting our data using a least-squares fit, we derive a star formation scale height of $z_{sfr} = 330 \pm 90$ pc (the red line in Fig. 7).

3.2 Displacement of HMXBs from star-forming regions

We observe in Fig. 7 that the star-forming activity is confined to the disc of NGC 55 with a scale height of 330 ± 90 pc, whereas the HMXBs are substantially extended beyond the SFR density. This suggests a 'puffed-up' population of HMXBs with respect to their birthplaces. The existence of a broadening in the spatial distribution of HMXBs is further shown in Fig. 8, where we overplot the location of HMXBs on images of NGC 55 that present different star formation tracers. In the top panel we show the 8.0 µm image (Dale et al. 2009) with the contribution from non-star-forming, stellar populations subtracted, as discussed in the previous section. In the middle panel, we show a *GALEX* NUV (2267 Å) image (Gil de Paz et al. 2007) that traces light from young stars. In the bottom panel is a starlight continuum subtracted Hα image obtained with the 4

Table 3. HMXB catalogue.

| RA (1)	Dec. (2)	z (3)	Flux (4)	$L_{x, 36}$ (5)
		Verified HMXBs		
00:14:19.2	−39:10:14.6	0.27	11.00	4.95
00:14:45.0	−39:10:53.7	0.29	1.80	0.81
00:14:47.3	−39:13:02.5	0.76	0.90	0.41
00:14:48.6	−39:12:15.9	0.31	1.20	0.54
00:14:50.9	−39:11:54.5	0.04	1.20	0.54
00:14:52.3	−39:12:06.0	0.09	2.90	1.31
00:14:52.5	−39:12:24.3	0.24	5.10	2.30
00:14:54.4	−39:12:44.8	0.36	1.00	0.45
00:14:56.7	−39:13:17.3	0.56	5.10	2.30
00:14:59.9	−39:12:49.1	0.20	2.00	0.90
00:15:00.6	−39:12:18.0	0.10	6.40	2.88
00:15:02.0	−39:11:45.5	0.43	1.20	0.54
00:15:11.9	−39:11:10.7	1.07	0.80	0.36
00:15:15.8	−39:15:08.7	0.88	1.90	0.86
00:15:22.2	−39:11:36.4	1.20	7.60	3.42
00:15:22.7	−39:14:52.7	0.50	0.80	0.36
00:15:23.3	−39:13:37.9	0.17	1.30	0.59
00:15:26.0	−39:12:56.3	0.63	1.10	0.50
00:15:33.9	−39:15:11.8	0.28	17.30	7.79
		Candidate HMXBs		
00 14 12.4	−39:10:17.8	0.43	9.00	4.05
00 14 19.3	−39:11:13.5	0.78	255.00	114.77
00 14 30.4	−39:12:57.8	1.24	18.70	8.42
00 14 38.5	−39:12:42.2	0.84	7.10	3.20
00 14 40.8	−39:09:37.8	0.87	10.70	4.82
00 14 43.6	−39:12:40.0	0.69	5.60	2.52
00 14 43.8	−39:11:27.4	0.00	3.30	1.49
00 14 46.8	−39:13:58.9	1.26	5.00	2.25
00 14 47.4	−39:09:44.1	0.99	2.00	0.90
00 14 49.8	−39:13:52.3	1.11	1.30	0.59
00 14 52.1	−39:13:34.3	0.84	1.90	0.86
00 14 52.5	−39:13:34.0	0.83	1.60	0.72
00 14 54.2	−39:13:32.1	0.75	0.90	0.41
00 14 54.5	−39:13:37.1	0.81	1.20	0.54
00 14 55.4	−39:09:46.1	1.25	1.40	0.63
00 14 57.1	−39:12:27.7	0.07	1.30	0.59
00 15 00.6	−39:14:14.2	0.92	1.10	0.50
00 15 01.5	−39:12:43.1	0.06	1.00	0.45
00 15 02.1	−39:14:25.2	0.97	2.90	1.31
00 15 03.4	−39:12:39.5	0.00	4.80	2.16
00 15 03.7	−39:12:41.4	0.00	0.80	0.36
00 15 04.2	−39:12:39.9	0.42	1.50	0.68
00 15 04.6	−39:10:50.5	1.00	4.10	1.85
00 15 05.3	−39:13:13.7	0.24	4.70	2.12
00 15 06.4	−39:12:46.0	0.07	0.80	0.36
00 15 07.6	−39:13:23.5	0.22	2.00	0.90
00 15 08.8	−39:11:18.0	0.94	1.10	0.50
00 15 13.6	−39:11 41.7	0.85	5.70	2.57
00 15 14.2	−39:13:20.6	0.04	3.00	1.35
00 15 14.8	−39:11:51.9	0.81	0.70	0.32
00 15 20.6	−39:12:19.5	0.79	1.20	0.54
00 15 28.1	−39:11:51.2	1.29	2.00	0.90
00 15 38.0	−39:12:32.8	1.25	17.50	7.88
00 15 42.1	−39:14:31.9	0.35	2.80	1.26
00 15 48.2	−39:16:13.9	0.34	7.10	3.20
00 15 48.2	−39:18:39.4	1.68	47.00	21.15
00 15 56.8	−39:13:39.7	1.30	11.60	5.22

Notes. Column description: (1) RA (hh:mm:ss) J2000, (2) Dec. (−dd:mm:ss) J2000, (3) vertical distance from the mid-plane (kpc), (4) flux (0.35–8 keV) in 10^{-15} erg s^{-1} cm^{-2}, and (5) luminosity (0.35–8 keV) in 10^{36} erg s^{-1}.
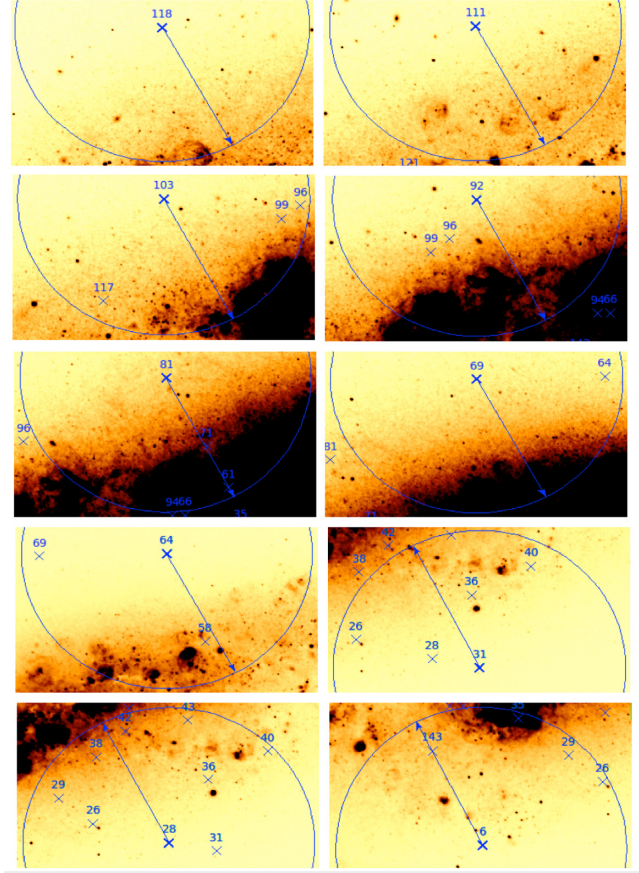
Figure 6. HMXBs located at large distances from the mid-plane superimposed on a starlight-subtracted Hα image (Kopsacheili et al. 2020) that traces star-forming regions. Each HMXB is indicated with an X and is encircled by a 1 kpc radius circle with the radial vector pointing towards the mid-plane of the galaxy. Individual HMXBs may be associated with any one of several star-forming regions.
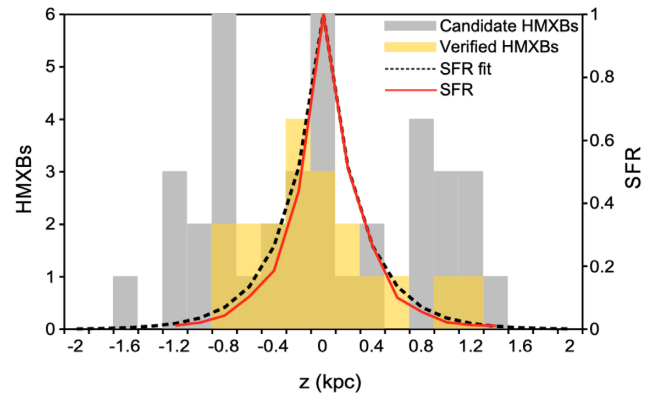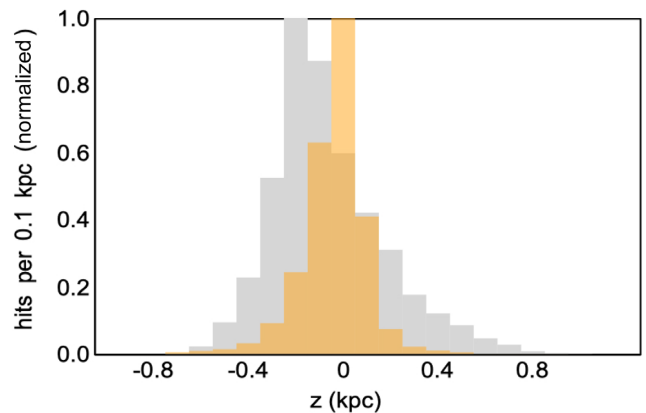

Figure 7. Vertical distribution of HMXB density in bins of 0.1×18 kpc (0.18 arcmin $\times$ 32 arcmin) from the mid-plane of NGC 55 (candidate and verified HMXBs in grey and yellow, respectively). The red line indicates the vertical distribution of the 8.0 μm based SFR density with the black line showing its best-fitting exponential profile. HMXBs extend beyond the star-forming region. North towards the positive values of z.
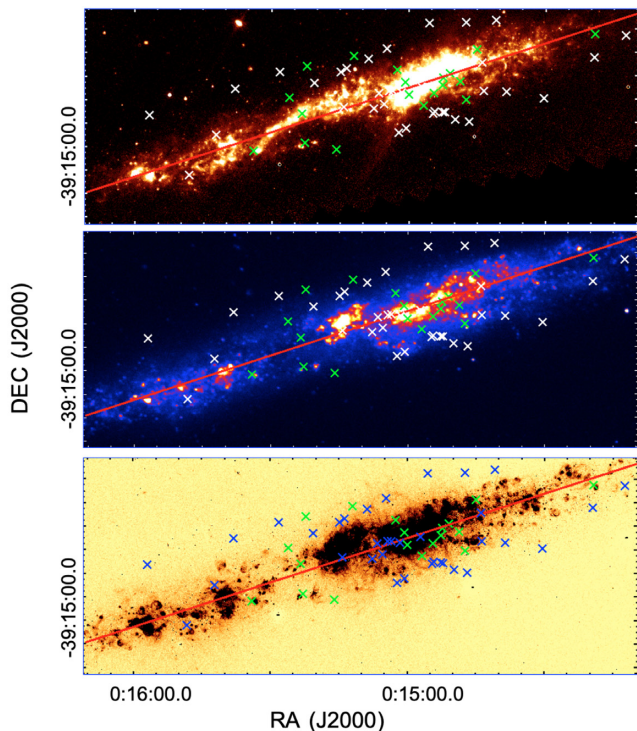
Figure 8. Locations of HMXBs and distribution of star formation in NGC 55 based on different star formation tracers. Top: 8.0 μm image (Dale et al. 2009) with the contribution from non-star-forming, stellar populations subtracted. Middle: *GALEX* NUV (2267 Å) image (Gil de Paz et al. 2007) that traces light from young stars. Bottom: Starlight continuum subtracted Hα image (Kopsacheili et al. 2020) tracing recent star formation. The red line depicts the mid-plane of NGC 55 as determined in Section 3.1. Candidate HMXBs are presented as white (top, middle panel) and blue (bottom panel) while verified HMXBs are presented as green in all panels. The HMXB population extends at large vertical offsets and at regions with relatively low star-forming activity.

m Blanco telescope at Cerro Tololo Inter-American Observatory (CTIO) (Kopsacheili et al. 2020) tracing recent star formation. The positions of HMXBs are shown as green, white, and blue circles in the top, middle, and bottom panels, respectively. In all three images, a significant fraction of XRBs is located beyond the extent of star formation activity and at large vertical offsets from the mid-plane.

We quantitatively examine the broadening in the spatial distribution of HMXBs by reconstructing the distribution of vertical offsets of HMXBs with respect to their birthplace by means of a Monte Carlo simulation. We sample randomly selected HMXB birth and current locations all drawn from the exponential distribution in equation (1), thereby creating virtual birthplaces and virtual locations of HMXBs. We measure the vertical offsets between virtual birthplaces and their nearest virtual HMXB location and produce a distribution that represents the null hypothesis that HMXBs are co-located with their parent star-forming region. We also measure the vertical offsets between virtual birthplaces and the nearest HMXB location from our HMXB sample and produce a distribution that represents the hypothesis that HMXBs are displaced from their parent star-forming region. We perform 10 000 iterations and calculate the distributions in 0.1 kpc bins. In order to account for the AGN contamination of 15 out of the 37 'candidate HMXBs' (Table 3), in each iteration our HMXB sample consists of randomly selected combinations of 22 out of 37 'candidate HMXBs', in addition to the 19 'verified HMXBs' (Table 3) for which no AGN

Figure 9. Distribution of HMXB vertical offsets calculated from Monte Carlo realizations of randomly selected birthplaces within the star-forming region. The distribution under the hypothesis that HMXBs are displaced from their parent star-forming region (the grey histogram) is extended compared with the distribution under the null hypothesis (the yellow histogram).

contamination is considered. The results are presented in Fig. 9. The distribution under the hypothesis that HMXBs are displaced from their parent star-forming region (the grey histogram) is extended compared with the distribution under the null hypothesis (the yellow histogram). Furthermore, a K-S test indicates the two populations are different at the 99.8 per cent confidence level.

We next quantify the observed displacement of HMXBs, which is attributed to kicks after an asymmetric SN explosion during the formation of the compact object (Fryer & Kalogera 1997). The contribution of natal kicks is treated as a Gaussian smearing function of standard deviation σ that broadens the spatial distribution of HMXBs compared with their birth distribution. We simulate the vertical distribution of HMXBs from the mid-plane as the convolution $P(z|\sigma, z_{sfr})$ between this Gaussian and the exponential distribution of SFR (equation 2) with a scale height of $z_{sfr} = 330$ pc .:

$$P(z|\sigma, z_{sfr}) = \sqrt{\frac{\pi\sigma^2}{2}} \exp\left(\frac{\sigma^2}{2z_{sfr}^2} - \frac{z}{z_{sfr}}\right)$$
$$\times \left[\text{erfc}\left[\sqrt{\frac{\sigma^2}{2}}\left(\frac{z}{\sigma^2} - \frac{1}{z_{sfr}}\right)\right]\right.$$
$$\left. - \exp\left(\frac{2z}{z_{sfr}}\right)\text{erfc}\left[\sqrt{\frac{\sigma^2}{2}}\left(\frac{z}{\sigma^2} + \frac{1}{z_{sfr}}\right)\right] - 2\right]. \quad (2)$$

We apply the maximum likelihood method for finding the best estimate of the Gaussian smearing parameter σ. The likelihood function $L(\mathbf{z}|\sigma, z_{sfr})$ derived from the convolution P is

$$L(\mathbf{z}|\sigma, z_{sfr}) = \prod_{i=1}^{N} P(z_i|\sigma, z_{sfr}), \quad (3)$$

where $N = 41$ is the number of HMXBs and z_i is the vertical distance of the ith HMXB from the mid-plane of NGC 55. We perform 100 000 iterations and in order to account for the estimated AGN contamination, in each iteration our HMXB sample consists of all 'verified HMXBs' (Table 3) as well as randomly selected combinations of 22 out of 37 'candidate HMXBs' (Table 3).

In Fig. 10 we show the likelihood of the dispersion of the Gaussian smearing function (normalized to the maximum likelihood). The maximum at $\sigma = 0.57 \pm 0.07$ kpc is the difference between the scale height of the vertical distribution of HMXBs and the
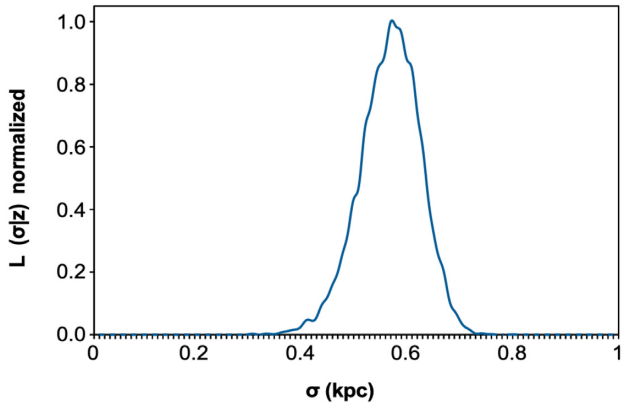
Figure 10. The likelihood of the dispersion of the Gaussian smearing function (normalized to the maximum likelihood σ), described in Section 3.2. The maximum at $\sigma = 0.57$ kpc is the scale height corresponding to the displacement between HMXBs and star-forming regions.
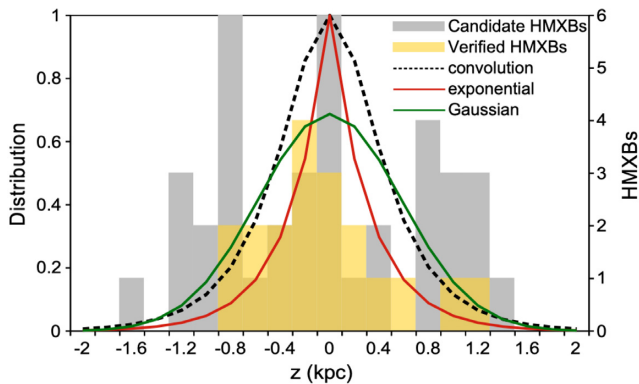
Figure 11. Simulated vertical distribution of HMXBs (black dashed) as the convolution between a Gaussian smearing function of standard deviation $\sigma = 0.57$ kpc (green) that represents the contribution of kicks, on top of the their birth distribution of 0.33 kpc (red). The grey and yellow histograms show the observed vertical distribution of candidate and verified HMXBs, respectively.

vertical distribution of star-forming activity. In Fig. 11 we show the simulated vertical distribution of HMXBs (black dashed line) as the convolution between a Gaussian smearing function of standard deviation $\sigma = 0.57$ kpc (green line) that represents the contribution of natal kicks, on top of their birth distribution of 0.33 kpc (red line).

3.3 Constraining the displacement of HMXBs

The result of the previous section mainly provides an upper limit on the scale height of HMXBs. There are other factors such as contamination, incompleteness and *in situ* formation of HMXBs that would bias the result of this analysis toward larger scale heights. We investigate these factors in an effort to constrain the lower limit on the scale height of HMXBs.

Although contamination from approximately 15 AGN interlopers from the 'candidate HMXBs' sample has been incorporated in the estimation of the scale height of HMXBs, we can make additional assumptions that constrain its effect towards lower scale heights. We first consider as interlopers the 15 'candidate HMXBs' with the largest distances from the mid-plane. Repeating

the analysis of Section 3.2 and excluding the 'candidate HMXBs' with the largest distances from the mid-plane, the resulting scale height of the vertical distribution of HMXBs is no less than 0.33 kpc.

We then make the hypothesis that all 'candidate HMXBs' are either AGN interlopers or misclassified LMXBs. By repeating the analysis of Section 3.2 including only the 'verified HMXBs', we find that the scale height of the vertical distribution of HMXBs is 0.39 kpc.

The other factor that would bias the results toward larger scale heights, is incompleteness at the low luminosities. There are three major effects leading to incompleteness.

The first derives from the dependence of the point response function on the off-axis angle. We expect this effect to be important at angular distances larger than 8 arcmin from the aimpoint (Wong et al. 2015). Since only four HMXBs from the sample of 'candidate' and 'verified' are located at distances larger than 8 arcmin from the aimpoint, incompleteness due to off-axis angle will only have a minor effect on our results.

The second effect has to do with the presence of diffuse emission (emission from hot inter-stellar medium or from unresolved faint sources). Stobbart, Roberts & Warwick (2006) investigated the diffuse emission of NGC 55 by extracting spectra representative of the residual disc emission and estimated the observed flux of the diffuse X-ray emission is at ~ 3 per cent of that of the resolved sources.

The third effect is caused by the high column density contours of 5×10^{21} cm^{-2} near the mid-plane (Stobbart et al. 2006), which makes absorption a potentially significant problem for the detection of HMXB candidates. To determine the impact of such absorption, we investigate the distribution of all X-ray sources (AGNs and XRBs) within the FOV in bins of 0.1 kpc from the mid-plane and perform a K-S test on the null hypothesis that their distribution is being drawn from a uniform one. At a confidence level of 95 per cent the estimated *X-rays (orange line), there is*-value of 0.8 per cent indicates that the distribution of all observed X-ray sources is not consistent with being flat, suggesting that the observed sources are not filling in for background ones that are not detected due to absorption, arguing for low incompleteness.

To quantitatively assess the effect of absorption through the edge-on star-forming gas disc of NGC 55, we assume that near the mid-plane at a distance of ± 1.2 kpc, which according to Davidge (2005), comprises the thin disc of NGC 55, most of the detected sources are those on the near side. To account for the sources on the far side that are possibly undetected due to absorption, we add sources at the same distances from the mid-plane as the observed ones and calculate the variation in the determination of the scale height. The results are presented in Fig. 12, where the maximum deviation from the observed scale height is approximately 20 per cent after the addition of 10 to 15 sources.

We also assume that for the observed X-ray sources located within the thin disc and detected in both the soft (0.3 $\rightarrow$ 1 KeV) and hard (2 $\rightarrow$ 7 keV) X-ray bands, emission from hard X-rays is less affected by absorption. In Fig. 13 we plot their luminosities in each band and in bins of 0.5 kpc vertical to the mid-plane. For the soft X-rays (the orange line), there is a significant decrease towards the northern part (0.5 kpc) of the galaxy. Emission from hard X-rays (the yellow line) is less affected and shows little variation as it passes through the thin disc. Assuming that the observed decrease in soft X-ray luminosity is caused by absorption, we quantify this at $\sim 3 \times 10^{37}$ erg s^{-1}. Since the average X-ray luminosity per source in the soft band is $\sim 2.5 \times 10^{36}$ erg s^{-1}, the estimated absorption affects the emission
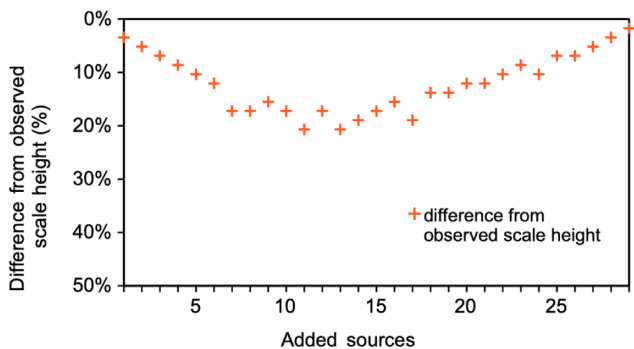
Figure 12. To account for the sources on the far side that are possibly undetected due to absorption, we add sources at the same distances from the mid-plane as the observed ones and calculate the variation in the determination of the scale height. The maximum deviation from the observed scale height is approximately 20 per cent after the addition of 10–15 sources.
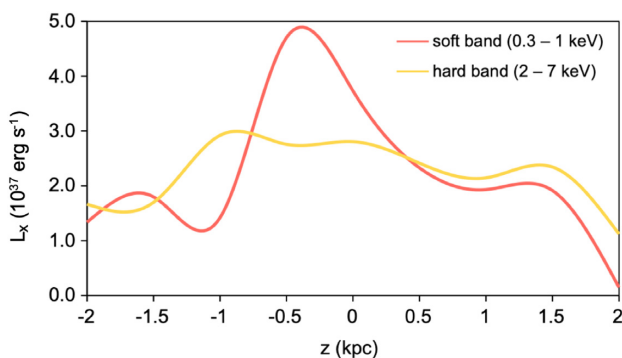

Figure 13. X-ray luminosities for sources detected in both the soft (0.3 → 1 KeV) and the hard (2 → 7 keV) bands in bins of 0.5 kpc vertical to the mid-plane. For the soft X-rays (the orange line), there is a significant decrease towards the northern part (0.5 kpc) of the galaxy which is estimated at $\sim 3 \times 10^{37}$ erg s^{-1}. Emission from hard X-rays (the yellow line) is less affected and shows little variation as it passes through the thin disc.

from approximately 12 undetected X-ray sources, in agreement with our previous assumption.

Regarding the *in situ* formation of HMXBs in extra-planar regions, we concentrate on the population of early type stars in NGC 55, where most OB stars are found close to the mid-plane (Kudritzki et al. 2016) with very little star-forming activity outside the main body of the disc (Davidge 2005). We estimate the ratio of the relative Hα flux in extra-planar to planar regions as a measure of the fraction of early type stars in each region (assuming the same SFR history). Defining the regions as in (Davidge 2005), with the planar at a height of 2.2 arcmin on either side of the mid-plane and the extra-planar falling between 2.2 and 4.4 arcmin off the mid-plane and using the starlight continuum subtracted Hα image of Section 3.1, the resulting ratio of only 6 per cent, suggests it is unlikely that more than one or two HMXBs may have been formed *in situ* at large latitudes.

From the analysis of the issues that would bias the scale height of the vertical displacement of HMXBs, it occurs that the lower limit on the scale height is estimated at 0.33 kpc, as a result of the exclusion of the 15 'candidate HMXBs' with the largest distances from the mid-plane as AGN interlopers. Furthermore, incompleteness can affect the upper and lower limits towards lower values by as much as 20 per cent.
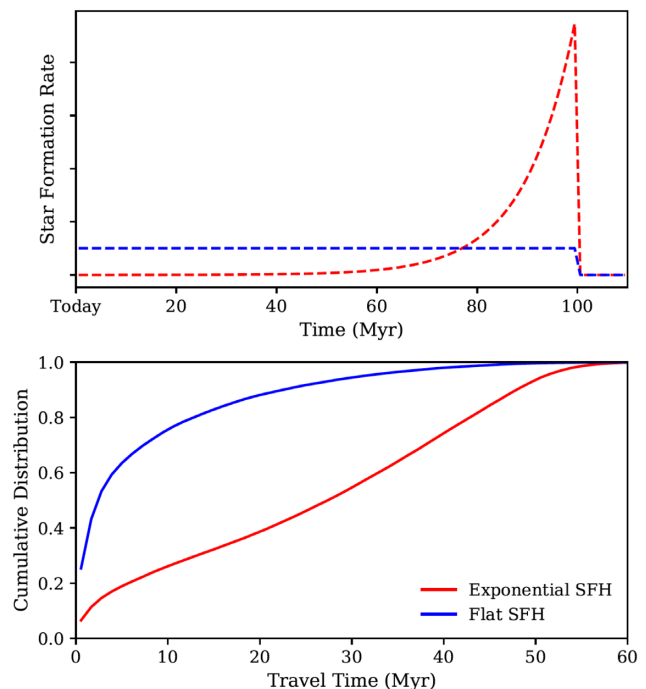
Figure 14. Top panel: Star formation history (SFH) models across the recent past of NGC 55. A flat model (blue dashed) where stars are formed at a constant rate and an exponentially declining model (red dashed) with a burst 100 Myr ago. Bottom panel: Cumulative distribution of HMXB traveltimes adopted from binary population synthesis codes for the flat (blue) and exponential (red) SFH models. Depending on the SFH, the traveltime and therefore the travel distance of HMXBs can substantially change.

3.4 Centre-of-mass transverse velocity of HMXBs

The companion stars of HMXBs are among the youngest stellar population in galaxies. Therefore the traveltime and distance of HMXBs depend on the recent star formation history of the galaxy. Since there are no published star formation histories for NGC 55, we adopt HMXB traveltimes predicted by binary population synthesis codes for two different SFH models (shown in the top panel of Fig. 14):

(1) A flat model where stars are formed at a constant rate.
(2) An exponentially declining model with a burst 100 Myr ago.

The SFHs are displayed in the top panel of Fig. 14 and are generated using a modified form of BSE, a binary population synthesis code described in Hurley, Tout & Pols (2002) with updates found in Andrews, Zezas & Fragos (2018) and its references. Default parametrizations and prescriptions are used. We use the statistical wrapper described in Andrews et al. (2018), to sample X-ray binaries with X-ray luminosities above 10^{36} erg s^{-1}. The synthetic populations are generated assuming different star formation histories, which we interpret as priors on our model distributions.

The vertical distance of HMXBs from the mid-plane is derived from the vertical distribution of stars corresponding to the star formation activity off the galaxy's plane (star-forming distance), added to the convolution between the traveltime and the centre-of-mass transverse velocity:

vertical distance = star-forming distance + [traveltime

$\times$ centre-of-mass transverse velocity

$\times \sin(\theta)\cos(\phi)$]

Table 4. HMXB centre-of-mass transverse velocity.

| HMXB sample | Velocity (km s^{-1}) | | Displacement (kpc) |
	Flat SFH	Exp. SFH	
Verified, candidate[a]	48 ± 9	22 ± 6	0.57 ± 0.07
Verified	41 ± 8	21 ± 6	0.39
Verified, candidate[b]	34 ± 7	20 ± 5	0.33

[a]Excluding 15 sources randomly selected; [b]excluding 15 sources with largest distances.
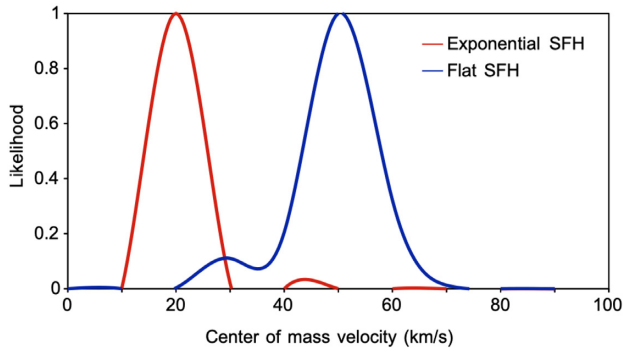
Figure 15. Normalized (to the maximum value) distribution of the centre-of-mass transverse velocity for the HMXB sample that consists of all 'verified HMXBs' as well as randomly selected combinations of 22 out of 37 'candidate HMXBs', for two different SFHs. For the exponential SFH model (tred line) the centre-of-mass transverse velocity is 22 ± 6 km s^{-1} and for the flhe at SFH model (the blue line) is 48 ± 9 km s^{-1}.

We assume the kick distribution to be isotropic, therefore the term $\sin(\theta)\cos(\phi)$ accounts for the random direction the kick will move the system, where θ is a polar angle that defines the angle between the kick velocity and the direction of orbital motion and is randomly drawn from $-1 < \cos(\theta) < 1$, while ϕ is an azimuthal angle randomly varying between 0 and 2π.

To determine the centre-of-mass velocity distribution, we reverse the previous equation: we combine the observed sample's vertical distribution with randomly drawn vertical distances off the plane of NGC 55 (according to the exponentially declining distribution of star formation), traveltime distributions (from binary population synthesis), and random polar and azimuthal angles to solve for the velocity distribution.

We determine the centre-of-mass velocity for the three cases we investigated in Sections 3.1 and 3.2. In the first case, the HMXB sample consists of all 'verified HMXBs' as well as randomly selected combinations of 22 out of 37 'candidate HMXBs'. In the second, the HMXB sample consists of 'verified HMXBs' only. In the third, we have the 'minimum' scale height sample, that consists of all 'verified HMXBs' and 'candidate HMXBs' excluding the 15 'candidate HMXBs' with the largest distances from the mid-plane. The results for the centre-of-mass transverse velocity of HMXBs are presented in Table 4.

Fig. 15 shows the centre-of-mass transverse velocity distribution (normalized to the maximum value) for the first case sample and for two different SFHs. For the exponential SFH model (red line) the centre-of-mass transverse velocity is 22 ± 6 km s^{-1} and for the flat SFH model (blue line) is 48 ± 9 km s^{-1}. For the second case, the 'verified HMXBs only' sample travels with a centre-of-mass transverse velocity of 22 ± 6 km s^{-1} for the exponential and 41 ± 8 km s^{-1} for the flat SFH model. For the third case, the 'minimum scale height' sample travels with a centre-of-mass

transverse velocity of 20 ± 5 km s^{-1} for the exponential and 34 ± 7 km s^{-1} for the flat SFH model.

4 DISCUSSION

In this work we try to constrain the centre-of-mass transverse velocity of HMXBs by using a statistical approach for estimating the displacement of HMXBs from their native star-forming location, as well as distributions from binary population synthesis codes for estimating the traveltime of HMXBs.

### 4.1 Displacement of HMXBs from star-forming regions

The HMXB population in our Galaxy provides an excellent benchmark for: (i) evaluating our statistical approach and (ii) comparing the vertical distribution of HMXBs between the two galaxies. Parallaxes from the second data release of *Gaia* (Gaia Collaboration 2018) allow us to measure their positions in the MW with unprecedented accuracy. We cross-correlate the HMXB catalogue of Liu et al. (2006) with the *Gaia* DR2 catalog and we find matches for 36 out of the 114 known Galactic HMXBs. One of these matches (1H 1936+541) is excluded because most likely it is associated with the bright galaxy cluster G086.45+15.29 at a redshift of 0.260 (Andrade-Santos et al. 2017). Sources without *Gaia* DR2 counterparts either lack a previously associated optical counterpart or are too extinct to be observed by *Gaia*. For the 35 HMXBs, we measure their vertical distances from the mid-plane of the Galaxy by adopting a distance of the Sun from the Galactic plane at $h = 17 \pm 5$ pc (Karim & Mamajek 2017).

We repeat the same statistical analysis as in Section 3.2 where we treat the contribution of kicks as a Gaussian smearing function of standard deviation σ that spreads the vertical distribution of HMXBs around the Galaxy plane when applied on top of the star formation activity distribution, which we consider is well represented by the vertical distribution of OB-stars in the Galaxy. We model the OB-stars distribution as an exponential function with a scale height of 103 ± 3 pc (Kong & Zhu 2008) and derive that the difference between the scale heights of the vertical distribution of HMXBs and the vertical distribution of star-forming activity is 36 ± 3 pc (Fig. 16).

To check the consistency of this result, we fit the distribution of vertical distances of HMXBs with an exponential function and find that the scale height of the vertical distribution of HMXBs in the Galaxy is 145 ± 23 pc (black dotted line in Fig. 14) in general agreement with previous estimates at: 150 pc (Grimm, Gilfanov & Sunyaev 2002b); 240^{+90}_{-40} pc (Dean et al. 2005); 134^{+39}_{-25} pc (Bodaghee et al. 2007); 85^{+23}_{-15} pc (Lutovinov et al. 2013). When compared with the scale height of the distribution of OB-stars as in the previous paragraph, the difference is at 42 ± 23 pc, consistent with the result from our statistical approach.

We note that from the distribution of HMXBs on the Galactic plane, Bodaghee et al. (2012) found much larger offsets between HMXBs and OB associations at 400 ± 200 pc, with nine HMXBs located more than 1 kpc from their nearest OB association. The difference between the vertical and horizontal offsets of the HMXBs distribution is consistent with the kinematics of stellar systems due to Galaxy rotation and the kinematics of X-ray binary systems: Prior to the SN explosion, the orbit of binary systems in disc galaxies lay on the plane of the disc. The SN explosion induces a kick in addition to the initial motion of the progenitor on the Galactic plane.

On the other hand, the vertical displacement of HMXBs in NGC 55 is greater than in the MW by an order of magnitude, despite
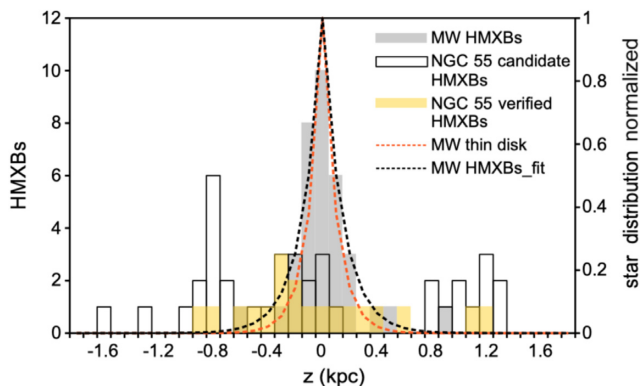
Figure 16. Vertical distribution of HMXBs in the MW (the grey histogram) along with the best-fitting exponential function (the black, dotted line) with a scale height of 145 ± 23 pc (Section 4). The red, dotted line presents the vertical distribution of OB-stars in the MW with a scale height of 103 ± 3 pc (Kong & Zhu 2008). Applying our statistical approach, we find that the difference between the scale heights of the two distributions is 36 ± 3 pc. The white and yellow histograms show the observed vertical distribution of candidate and verified HMXBs in NGC 55. Despite the similar kick velocities the HMXBs receive in both galaxies, the distribution of vertical displacements in NGC 55 is much wider. We attribute the difference to the greater gravitational potential and therefore greater escape velocity of the Galactic disc that confines HMXBs more closely to the Galactic plane.

the similar kick velocities the HMXBs receive in both galaxies. We attribute this difference to the greater gravitational potential of the MW that confines HMXBs more closely to the Galactic plane. More specifically, the stellar mass of NGC 55 is at $1.94 \times 10^9 \, M_\odot$ (Kudritzki et al. 2016) while for the Galaxy is 25 times greater, at $5.76 \times 10^{10} \, M_\odot$ (Licquia & Newman 2004). The local Galactic escape speed is estimated at 533 km s^{-1} (Piffl et al. 2014), while the escape velocity for NGC 55, using similar gravitational potential profiles as for the MW, is estimated at $\sim$100 km s^{-1}, which is consistent with the distribution of transverse velocities of HMXBs in NGC 55 (Fig. 15). The typical kick velocities are well below the escape velocity of NGC 55, suggesting that most systems ought to remain bound to their host potential.

4.2 Centre-of-mass transverse velocity of HMXBs

Measurements of the transverse velocities of HMXBs in the MW and the MCs correlate the traveltime with the maximum lifetime of the companion Be star after the creation of the NS (taking into account the fact that the Be phenomenon appears towards the end of the main-sequence lifetime of a B-type star) which is estimated using models for the evolution of massive stars in binary systems. These measurements show that the centre-of-mass transverse velocity of HMXBs is 12.4 ± 7.0 km s^{-1} for the LMC (Antoniou & Zezas 2016) and 16 km s^{-1} for the SMC (Coe 2005). The corresponding space velocities are 17.5 ± 9.8 km s^{-1} for the LMC (Antoniou & Zezas 2016) and 30 km s^{-1} for the SMC (Coe 2005). For the MW, where van den Heuvel et al. (2000) derived proper motions from *Hipparcos* measurements, the transverse velocity of four SG-XRBs is 42 ± 14 km s^{-1} and of 13 Be-XRBs is 15 ± 6 km s^{-1}. On the other hand, Bodaghee et al. (2012) used a sample of 79 Galactic HMXBs and estimated an average space velocity of 100 ± 50 km s^{-1}.

In this study we follow a different approach and use traveltime distributions (Fig. 14) derived from binary population synthesis

codes based on different SFH models. We find that for a flat SFH model, which is typical of spiral galaxies like NGC 55, HMXBs are moving with typical transverse velocities between 34 and 48 km s^{-1}, consistent with space velocities of MW HMXBs.

For an exponential SFH model, with a starburst 100 Myr ago, HMXBs in NGC 55 have somewhat lower transverse velocities of approximately 21 km s^{-1}, consistent with the corresponding transverse velocity of HMXBs in the SMC and LMC.

Assuming that NGC 55 is reasonably accurately modelled with a flat SFH, our results show that despite the similar kicks the HMXBs receive, the induced centre-of-mass velocities are higher in NGC 55 than in the MCs. The differences can be attributed to pre- and post-SN orbital characteristics from which we can enrich our insight into the evolutionary process of XRB systems and revise the parameter space of theoretical models to reproduce the higher velocities by considering: (i) Higher pre-SN orbital velocities (Brandt & Podsiadlowski 1995). (ii) Larger masses of the secondary star (Brandt & Podsiadlowski 1995). (iii) Larger amounts of mass ejected during the SN explosion (Brandt & Podsiadlowski 1995). (iv) Increased natal kick velocities that also affect the fraction of systems that remain bound (Kalogera 1996). We note that regardless of possible kick velocities, the combination of (i)–(iii) leads to a considerable difference in the velocities between SG-XRBs and Be-XRBs (van den Heuvel et al. 2000). The comparatively high spatial velocities of HMXBs in NGC 55 suggest a larger fraction of SG-XRBs in NGC 55 than in the MW and also hint for a small fraction of electron-capture SNe that impart very small kicks (Linden et al. 2009).

4.3 HMXB formation efficiency and metallicity

The formation rate of HMXBs follows closely the local SFR and metallicity (Fragos et al. 2013; Antoniou et al. 2019). Since there is no local SFR data for NGC 55, we compare the HMXB formation efficiency in NGC 55 with the relevant efficiency in the SMC, LMC, and the MW, based on the average SFR of each galaxy (Table 4). We find that down to a luminosity of $L_x = 0.3 \times 10^{36}$ erg s^{-1} the HMXBs/SFR in NGC 55 is 299^{+50}_{-46} (systems/M$_\odot$ yr^{-1}) assuming 41 HMXBs, which we consider as the most probable number of HMXBs in NGC 55 and SFR measurements from Weisz et al. 2011. In the case of LMC and SMC, down to a luminosity of $L_x = 3 \times 10^{33}$ erg s^{-1} (Antoniou & Zezas 2016) we have 160^{+96}_{-64} (systems/M$_\odot$ yr^{-1}) and 480^{+400}_{-240} (systems/M$_\odot$ yr^{-1}) respectively (Harris & Zaritsky 2009; Antoniou & Zezas 2016). For the MW we have 69 ± 17 (systems/M$_\odot$ yr^{-1}; Bodaghee et al. 2012; Licquia & Newman 2004). The errors are based on error propagation from the number of X-ray sources and the uncertainty on the SFR. The formation rate for the LMC and SMC is consistent with those calculated by Antoniou & Zezas (2016b) given the local SFR of the episodes responsible for the formation of HMXBs. Taking into consideration the metallicity in each galaxy (Table 5), we see that the number of HMXBs per SFR is higher in galaxies with subsolar metallicity. This is consistent with binary population synthesis models predicting more efficient HMXB production in metal poor environments (Linden et al. 2010; Fragos et al. 2013), where the fraction of binaries disrupted by the SN explosion is lower (Renzo et al. 2019).

5 CONCLUSIONS

We present a systematic study of the vertical distribution of HMXBs in the edge-on galaxy NGC 55 with respect to the distribution of

Table 5. Comparison of HMXB displacement in different galaxies.

	LMC	SMC	MW	NGC 55
Average displacement (kpc)	0.09 ± 0.05^a	0.07^b	0.40 ± 0.20^c	$0.33–0.57^d$
Average velocity (km s^{-1})	SG-XRBs 12.4 ± 7.0^a	16^b	SG-XRBs 42 ± 14^l	21^m
	Be-XRBs 10.8 ± 7.3^a	13.1^a	Be-XRBs 15 ± 6^l	$34–48^n$
Metallicity (Z$_\odot$)	0.4^a	0.2^a	1	0.4^e
SFR (M$_\odot$ yr^{-1})	$0.25^{+0.15\,f}_{-0.10}$	$0.30^{+0.55\,f}_{-0.15}$	1.66 ± 0.20^h	$0.137^{+0.023\,k}_{-0.021}$
Stellar mass (M$_\odot \times 10^9$)	2.70^g	0.31^g	57.6^h	1.94^i
HMXBs	40^a	144^a	114^c	41^j
HMXBs/SFR (systems/M$_\odot$ yr^{-1})	160^{+96}_{-64}	480^{+400}_{-240}	69 ± 17	299^{+50}_{-46}

^{a}Antoniou & Zezas (2016); ^{b}Coe (2005); ^{c}Bodaghee et al. (2012); ^{d}this study; ^{e}Kudritzki et al. (2016); ^{f}Harris & Zaritsky (2009); ^{g}van der Marel, Kallivayalil & Besla (2009); ^{h}Licquia & Newman (2004); ^{i}Kudritzki et al. (2016); ^{j}this study based on Binder et al. (2015); ^{k}Weisz et al. (2011); ^{l}van den Heuvel et al. (2000); ^{m}this study, for an exponential SFH; ^{n}this study, for a flat SFH

star-forming activity. We find evidence for an extended distribution of HMXBs compared to the star-forming activity distribution. The maximum likelihood scale height corresponding to the displacement between HMXBs and star-forming regions is between 0.33 and 0.57 kpc. We interpret the vertical offsets in the context of a momentum kick during the SN explosion of the primary star that leads to the formation of a neutron star.

Using HMXB traveltimes from binary population synthesis codes for different SFH models we find that the centre-of-mass transverse velocity strongly depends on the recent SFH of NGC 55. For a flat SFH model the centre-of-mass is moving at a velocity between 34 and 48 km s^{-1}, consistent with velocities of MW HMXBs, while for an exponential SFH model the centre-of-mass is moving at a velocity of approximately 21 km s^{-1}, consistent with the corresponding velocity of HMXBs in the SMC and LMC. Furthermore, the formation efficiency of XRBs in NGC 55 is consistent with the formation efficiency of XRBs in SMC and LMC, but significantly larger than that of the MW, a difference that can be attributed to the subsolar metallicity of both the MCs and NGC 55. A summary of our results as well as the corresponding values for the LMC, SMC, and the MW is presented in Table 5.

REFERENCES

Andrade-Santos F. et al., 2017, ApJ, 843, 76
Andrews J. J., Zezas A., Fragos T., 2018, ApJS, 237, 1
Antoniou V., Zezas A., 2016, MNRAS, 459, 528
Antoniou V. et al., 2019, High-mass X-ray Binaries: Illuminating the Passage from Massive Binaries to Merging Compact Objects. Proc. IAU Symp. vol. 346, Cambridge University Press, Cambridge, 316
Bhattacharya D., van den Heuvel E. P. J., 1991, Phys. Rep., 203, 1
Binder B. et al., 2015, AJ, 150, 94
Bodaghee A., Tomsick J. A., Rodriguez J., James J. B., 2012, ApJ, 744, 108
Bodaghee A. et al., 2007, A&A, 467, 585
Brandt N., Podsiadlowski P., 1995, MNRAS, 274, 461
Calzetti D., 2008, in Chary R.-R., Teplitz H. I., Sheth K., eds, ASP Conf. Ser. Vol. 381, Infrared Diagnostics of Galaxy Evolution. Astron. Soc. Pac., San Francisco, p. 323
Castro N. et al., 2008, A&A, 485, 41
Coe M. J., 2005, MNRAS, 358, 1379
Dalcanton J. J. et al., 2009, ApJS, 183, 67
Dale D. A. et al., 2009, ApJ, 703, 517
Davidge T. J., 2005, ApJ, 622, 279
Dean A. J. et al., 2005, A&A, 443, 485
de Vaucouleurs G., de Vaucouleurs A., Corwin H. G., Jr., Buta R. J., Paturel G., Fouqué P., 1991, Third Reference Catalogue of Bright Galaxies. Volume I: Explanations and references. Volume II: Data for galaxies between 0^h and 12^h. Volume III: Data for galaxies between 12^h and 24^h. Springer Science+Business Media, New York, USA
Ekström S. et al., 2012, A&A, 537, A146
Engelbracht C. W. et al., 2004, ApJS, 154, 248
Fabbiano G., 2006, ARA&A, 44, 323
Fragos T. et al., 2013, ApJ, 764, 41
Fryer C., Kalogera V., 1997, ApJ, 489, 244
Gaia Collaboration 2018, A&A, 616, A1
Gieren W., Pietrzyński G., Soszyński I., Bresolin F., Kudritzki R.-P., Storm J., Minniti D., 2008, ApJ, 672, 266
Gil de Paz A. et al., 2007, ApJS, 173, 185
Grimm H.-J., Gilfanov M., Sunyaev R., 2002b, A&A, 391, 923
Grimm H.-J., Gilfanov M., Sunyaev R., 2003, MNRAS, 339, 793
Harris J., Zaritsky D., 2009, AJ, 138, 1243
Hurley J. R., Tout C. A., Pols O. R., 2002, MNRAS, 329, 897
Jarrett T. H., 2000, PASP, 112, 1008
Kaaret P., Alonso-Herrero A., Gallagher J. S., Fabbiano G., Zezas A., Rieke M. J., 2004, MNRAS, 348, L28
Kalogera V., 1996, ApJ, 471, 352
Karim M. T., Mamajek E. E., 2017, MNRAS, 465, 472
Khan R., Stanek K. Z., Kochanek C. S., Sonneborn G., 2015, ApJS, 219, 42
Kim M. et al., 2007, ApJS, 169, 401
Kong D.-L., Zhu Z., 2008, Chin. Astron. Astrophys., 32, 360
Kopsacheili M., Zezas A., Liodaki I., 2020, MNRAS, 491, 889
Kudritzki R. P., Castro N., Urbaneja M. A., Ho I.-T., Bresolin F., Gieren W., Pietrzyński G., Przybilla N., 2016, ApJ, 829, 70
Licquia T., Newman J., 2004, Am. Astron. Soc., 223, 336.04
Linden T., Kalogera V., Sepinsky J. F., Prestwich A., Zezas A., Gallagher J. S., 2010, ApJ, 725, 1984
Linden T., Sepinsky J. F., Kalogera V., Belczynski K., 2009, ApJ, 699, 1573
Liu Q. Z., van Paradijs J., van den Heuvel E. P. J., 2006, A&A, 455, 1165
Lutovinov A. A., Revnivtsev M. G., Tsygankov S. S., Krivonos R. A., 2013, MNRAS, 431, 327
Miller S. T., Veilleux S., 2003, ApJ, 592, 79
Okazaki A. T., Hayasaki K., Moritani Y., 2013, PASJ, 65, 41
Persic M., Rephaeli Y., 2007, A&A, 463, 481

Pfahl E., Rappaport S., Podsiadlowski P., Spruit H., 2002, ApJ, 574, 364

Piffl T. et al., 2014, A&A, 562, A91

Podsiadlowski P., Langer N., Poelarends A. J. T., Rappaport S., Heger A., Pfahl E., 2004, ApJ, 612, 1044

Porter J. M., Rivinius T., 2003, PASP, 115, 1153

Reig P., 2011, Ap&SS, 332, 1

Seth A. C., Dalcanton J. J., de Jong R. S., 2005, AJ , 130, 1574

Stern D. et al., 2005, ApJ, 631, 163

Renzo M. et al., 2019, A&A, 624, A66

Stobbart A.-M., Roberts T. P., Warwick R. S., 2006, MNRAS, 370, 25

van den Heuvel E. P. J., Portegies Zwart S. F., Bhattacharya D., Kaper L., 2000, A&A, 364, 563

van der Marel R. P., Kallivayalil N., Besla G., 2009, in Van Loon J. T., Oliveira J. M., eds, IAU Symposium Vol. 256, The Magellanic System: Stars, Gas, and Galaxies. Cambridge Univ. Press, Cambridge, p. 81

van Rensbergen W., Vanbeveren D., De Loore C., 1996, A&A, 305, 825

Weisz D. R. et al., 2011, ApJ, 739, 5

Westmeier T., Koribalski B. S., Braun R., 2013, MNRAS, 434, 3511

Williams S. J., Bonanos A. Z., 2016, A&A, 587, A121

Williams S. J., Bonanos A. Z., Whitmore B. C., Prieto J. L., Blair W. P., 2015, A&A, 578, A100

Wong R. K. W., Kashyap V. L., Lee T. C. M., van Dyk D. A., 2016, The Annals of Applied Statistics, 10, 1107

Wu H., Cao C., Hao C.-N., Liu F.-S., Wang J.-L., Xia X.-Y., Deng Z.-G., Young C. K.-S., 2005, ApJ, 632, L79

Zezas A., Fabbiano G., Rots A. H., Murray S. S., 2002, ApJ, 577, 710

This paper has been typeset from a TEX/LATEX file prepared by the author.